学的な性質と生体側の解剖学的・生理学的特性とのバランスで受動的に規定される現象を利用してデリバリーを行うもので，標的との特異的な相互作用は利用しない。例えば合成高分子をキャリアとしてターゲティングを行う場合，合成高分子の分子量，親水性/疎水性，荷電状態といった物理的・化学的要素によって，このキャリアシステムの体内動態と分布を制御するのである。

さて，ここで話題を元に戻し，薬物ターゲティングと画像診断の関係について抗癌剤ターゲティングを例として述べる。癌へのターゲティングが達成されることは，癌成長抑制測定による抗癌活性評価と，癌細胞・組織への抗癌剤（あるいはキャリアシステム）の集積によって実証される。抗癌剤の癌ターゲティングの実証は，癌組織を取り出して薬物量をHPLCで測定したり，放射能を測定したり，病理切片を顕微鏡観察することが中心で，MRIやSPECT画像を用いる例は少ない。臨床になると，画像診断によってターゲティングを実証する治験（抗癌剤投与と外科切除併用の治験のような）は稀である。もちろん，臨床において抗癌剤の効果を投与前後の画像診断を用いて評価する（癌の縮小を定量して）ことはあっても，ターゲティングを可視化することを通して，薬物ターゲティングと画像診断が直接に関係することが稀なのである。この原因の1つとしては，薬物ターゲティングと画像診断に共通するキャリアシステムが多くないことが挙げられる。

Ⅱ．分子イメージングを通した薬物ターゲティングと画像診断の技術的融合

ここで，薬物ターゲティングと分子イメージングの関係について2つ述べたい。第一に，ターゲティングは，前述したアクティブターゲティングとパッシブターゲティングの両者ともその選択性の原理は分子イメージングと共通することである。病変細胞に特異的に発現したリガンド分子に結合する抗体を利用した例を考えれば，アクティブターゲティングが分子イメージングと同じ原理であることは自明であるが，パッシブの場合も生体分子に基づく現象を基盤としている場合には，分子イメージングと選択性の原理が共通する。この好適な例は，固形癌ターゲティングのEPR効果[2)3)用解1]である。EPR効果（enhanced permeability and retention effect）とは，固形癌では血管の透過性亢進と，リンパ系による排出抑制によって，ナノサイズのキャリアが本質的に固形癌組織に選択的に蓄積しやすい性質で，これに基づいて固形癌組織へのパッシブターゲティングが可能となる。この癌組織血管の透過性亢進はVEGFやキニンといった分子によって引き起こされるものであり，特定の分子が引き起こす状態変化を可視化する分子イメージングとは原理を共通すると言えるのである。

第二は，薬物ターゲティングと分子イメージングは歴史的には全く別個と言ってもよい発展の道をたどってきたことである。DDSのターゲティング研究では，動物の体内分布測定のための画像を撮ることはあっても，それをヒトの診断技術として実用化しようとする研究は1990年代まではほとんどなかった。MRI造影剤では，デキストラン[4)]，アルブミン[5)]，リポソーム[6)]にキレート化合物を結合・内封させることによる高分子型のMRI造影剤研究が1980年代からわずかに行われていたにすぎない。また，特異抗体に放射性同位元素を標識した複合体を用いる画像診断と，抗癌剤などの薬物を抗体に結合して行うターゲティングには，（意外と感じられるかもしれないが）技術的な重なりはあまりない。薬物ターゲティングでは，薬効を高めるために抗体分子あたり，なるべく多くの薬物を結合させてもターゲティング能を低下させないための技術開発が行われてきた。一方，抗体-放射性同位体では，結合させる同位体の量はわずかですむために，薬物ターゲティングで得られた技術を使う必要がなかったからである。

この状況が一変するのは，最近10年くらいの分子イメージング研究開発の急速な発展があったためである。薬物ターゲティングのキャリア技術が分子イメージングで使われたり，ターゲティング効果の証拠に分子イメージングが使われたりすることが積極的に行われるようになった。前述したように，薬物ターゲティングと分子イメージン

図❶　分子イメージングの進展による薬物ターゲティングと画像診断の緊密化

グの両者は特定の細胞・組織・臓器への選択性・特異性で共通することは自明である。また，図❶に示すように技術的には分子イメージング研究・開発の1つの特長である多様な画像モダリティが，両者を関係づける鍵になったと私は考える。画像診断側からは，多様なモダリティに対応しうる造影剤システム作製に薬物キャリアの技術が必要となった一方，ターゲティングの実証のための画像の利用範囲が飛躍的に広がったためである。両領域とも臨床試験およびそれを見据えた開発が盛んになっている現在が，両領域を組み合わせた研究開発が行われる価値がある時期であると私は信ずる。

Ⅲ. 薬物ターゲティング技術の分子イメージングへの応用

1．薬物ターゲティングとイメージングの違い

キャリアを用いて薬物と造影剤を標的部位に選択的に送達することは薬物と造影剤では共通するのであるが，この2つの領域で異なる要素が2つある。

(1) 送達する量の問題

まず例として特異抗体を用いて抗癌剤を運ぶ場合（DDS）と放射性同位元素を運ぶ場合（イメージング）を比較する。多くの抗癌剤のヒト1人の投与量は数十 mg から数百 mg であり，抗体に結合してターゲティングすることでは，実はこの投与量はかなり多いと認識すべき量なのである。抗体の機能を高いレベルで保持するためには，抗体1分子あたりに結合する薬物分子をなるべく少なくしたほうがよいが，そうなると用いる抗体量が大きなものとなってしまい，抗体自身の副作用が問題となる。例えば，分子量500で投与量が50mgの抗癌剤を分子量16万の抗体分子に5分子結合する場合を想定すると，投与する抗体量は3.2gにも及ぶ〔事実，抗体と抗癌剤の結合体で唯一認可を得ているゲムツズマブオゾガマイシン（マイロターグ®）は殺細胞活性が非常に強い抗癌剤を用いることで，投与する抗体量が少ないこと（成人で15mg程度）が1つの成功要因と思われる〕。

これとは対照的に，イメージングのための放射性同位元素は投与量が小さくてすむために，抗体の投与量の問題が生じることはない。しかし，造影剤でも Gd イオンなどの MRI 造影剤はその投与量は放射性同位元素に比べて大きく，DDS の場合と同様にキャリアの投与量の問題は起こりうる。

量に関する第二の点は，造影剤の場合には標的に到達させるべき割合が相対的であることである。抗癌剤のターゲティングの場合には，投与量のうちどれくらいの割合が癌に送達されないとターゲティング効果が発揮されないという最低割合が存在ずる。癌以外の正常部位に到達したものは副作用を起こすので，癌へ到達する割合を高めることが重要なのである。造影剤の場合には，造影に必要な絶対量（投与量に対する割合でなく）が送達され，その時に標的と見分けるべき部位の送達量が十分に低ければよい。この見分けるべき部位が血管（血液）である場合には，抗癌剤の場合に問題となる正常組織・臓器への分布は無視できることとなる。よって，同一の送達効率のキャリアを造影剤と抗癌剤で共通に用いても，片方の場合のみで用いる意義があることが十分想定できるのである。

(2) 毒性

異なる第二の点は毒性である。治療と診断では許容される毒性が大きく異なるのは自明なことで

図❷　高分子ミセルをキャリアとした造影剤と薬物ターゲティングシステム

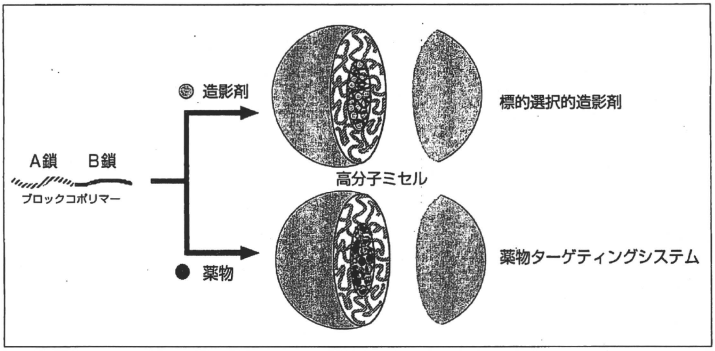

図❸　高分子ミセル造影剤と高分子ミセル抗癌剤の体内動態・分布の比較

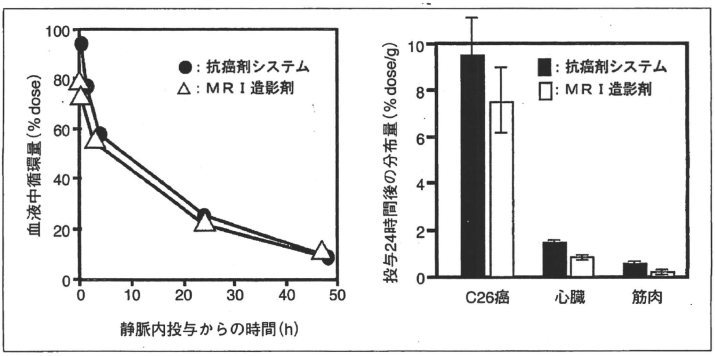

ある。抗癌剤治療ではかなり重篤な副作用の出現も許容される場合があるが，対象が癌であっても診断目的では，重篤な副作用は限りなくゼロに近づけることが求められる。よってキャリア自体の毒性も，抗癌剤ターゲティングでは問題にならないレベルでも，造影剤を対象とした場合には大きな問題となることがありうる。

2．薬物と造影剤をターゲティングする高分子ミセルキャリア

最後に筆者らが高分子ミセルキャリアを用いた抗癌剤とMRI造影剤ターゲティングの例を紹介させていただく。「高分子ミセル」とはその名のとおり，高分子からなるミセル構造のことである。典型的には図❷に示すような形態のAB型ブロックコポリマーから形成され，ミセル外殻を形成する水溶性の高分子鎖としては，ポリエチレングリコール（PEG）を用いる。このブロックコポリマーが，数十～数百個会合して直径が数十nmのミセル構造を形成する。A鎖は親水性の外殻を構成し，B鎖は薬物あるいは造影剤成分の封入の役割を担う。ミセルへの導入は，B鎖に化学的に結合するか，B鎖が形成するミセル内核に物理的に主に疎水性相互作用で封入させる。

高分子ミセルMRI造影剤の一例は，ポリエチ

図❹　診断・治療が融合した癌医療システム

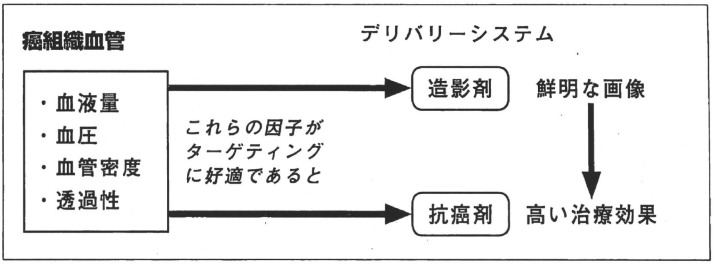

レングリコール-b-ポリアスパラギン酸ブロックコポリマーのアスパラギン酸残基にキレート基であるDOTAを結合させたもので作製される。水のT1緩和時間を短縮することによりMRIコントラストをもたらすGdイオンをこのブロックコポリマーのDOTA基に配位したものは，ポリアスパラギン酸誘導体ブロック同士の相互作用によって，高分子ミセルを形成する。高分子鎖長，Gdイオンの配位数を制御したところ，図❸に示すように，マウスC26癌に選択性高くターゲティングすることができた[7]。この動態と分布は，抗癌剤ドキソルビシン（アドリアマイシン®）を内包した高分子ミセルシステム[8]と極めて類似したものであった。この結果から，2つの臨床的な可能性が期待される。その第一は，EPR効果に基づいて，従来では発見できなかった微小な癌の早期発見を可能にすることである。第二には，抗癌剤治療の効果を個々人で予想しうる診断システムを構築することである。図❹に示すように，EPR効果に基づくターゲティングの重要な因子は癌組織血管の密度・透過性と，その血管の中を流れる血液量･圧力である。これらの因子が癌ターゲティングに好ましい患者では，高分子ミセル造影剤によってより鮮明な画像が得られ，高分子ミセル抗癌剤ターゲティングシステムによる高い治療効果がきたされる。よって，この造影剤で癌が明瞭に造影できた患者は，同じ高分子ミセルキャリア治療が高い効果であると予想することが成立する。もちろん，この予想が成立（すなわち医療として認可される）するためには，抗癌剤単独の臨床試験のみでは不十分で，この組み合わせ医療としての有効性を実証する必要がある。

このような診断と治療が組み合わされた癌医療は他にはなく，高い医療価値が期待される。ただし，PEGを成分として含むナノサイズの製剤で知られているABC（accelerated blood clearance）現象[9][10]が理論的には問題となりうる。このABC現象はPEG修飾リポソームでよく知られており，二度目の投与では免疫的な作用によって，極めて迅速に血液から除かれてしまってターゲティング性能が発揮できなくなることである。もし，造影剤の一度目の投与でABC現象が引き起こされると，二度目の抗癌剤治療の効果が大幅に減少する問題がある。幸いなことに，高分子ミセル造影剤はPEGを有するのであるが，典型的な条件でABC現象を引き起こさない[11]。また，薬物ターゲティング用の高分子ミセルキャリアも，ABC現象を引き起こさないものがあることがわかってきた。ABC現象については今後ともに詳細な検討を続ける必要があるが，高分子ミセル造影剤はこの免疫学的な点でも利点を有することが明らかとなった。

おわりに

薬物ターゲティングと分子イメージングの両領域が，活発な情報交換と共同研究を通して画像診断と薬物治療，基礎と臨床の両側面で大いに発展が望める条件が現在揃っていると，筆者は考える。また，その発展が必要とされているのも現在であるともいえる。

用語解説

1. **EPR効果**：固形癌組織へ受動的にターゲティングする原理。enhanced permeability and retention effectの略。癌組織では血管内皮の透過性が異常に亢進していると同時に，リンパ系による排出が抑制されているために，ナノサイズのキャリアが本質的に固形癌部位に選択的に集積すること。この方式によるターゲティングには，癌細胞の特異抗原に対する抗体のような，特異的リガンドは必要ない。1986年に前田，松村によって提唱された。

参考文献

1) Yokoyama M, et al : Adv Drug Deliv Rev 21, 77-80, 1996.
2) Matsumura Y, Maeda H : Cancer Res 46, 6387-6392, 1986.
3) Maeda H, Seymour LW, et al : Bioconjug Chem 3, 351-362, 1992.
4) Wang SC, Brasch RC, et al : Radiology 175, 483-488, 1990.
5) Schmiedel U, Brasch RC, et al : Invest Radiol 22, 713-721, 1987.
6) Unger E, Tilcock C, et al : Invest Radiol 25, 638-644, 1990.
7) Shiraishi K, Yokoyama M, et al : J Control Release 136, 14-20, 2009.
8) Yokoyama M, Okano T, et al : J Drug Target 7, 171-186, 1999.
9) Dams ET, Storm G, et al : J Pharmacol Exp Ther 292, 1071-1079, 2000.
10) Ishida T, Kiwada H : Int J Pharm 354, 56-62, 2008.
11) Ma H, Shiraishi K, et al : Pharm Res 27, 296-302, 2010.

横山昌幸

1989年　東京女子医科大学医用工学研究施設助手
1993年　米国スクリプス研究所へ留学（～1995年）
1996年　東京女子医科大学医用工学研究施設講師
2001年　同大学先端生命医科学研究所遺伝子医学分野助教授
2004年　神奈川科学技術アカデミー横山ナノバイオテクノロジープロジェクトリーダー
2009年　東京慈恵会医科大学総合医科学研究センター医用ナノシミュレーション研究室准教授

専門：機能性高分子，バイオマテリアル，ドラッグデリバリーシステム，ウイルス免疫学

International Journal of Pharmaceutics 404 (2011) 271–280

Contents lists available at ScienceDirect

International Journal of Pharmaceutics

journal homepage: www.elsevier.com/locate/ijpharm

Pharmaceutical Nanotechnology

Effects of organic solvents on drug incorporation into polymeric carriers and morphological analyses of drug-incorporated polymeric micelles

Yoshiko Harada[a], Tatsuhiro Yamamoto[b], Masaru Sakai[c], Toshiharu Saiki[c,d], Kumi Kawano[e], Yoshie Maitani[e], Masayuki Yokoyama[b,f,*]

[a] Japan Science and Technology Agency, ERATO, Takahara Soft Interfaces Project, CE80, Kyushu University, 744 Motooka, Nishi-ku, Fukuoka 819-0395, Japan
[b] Yokoyama Nanomedical Project, Kanagawa Academy of Science and Technology, KSP East 404, 3-2-1 Sakado, Takatsu-ku, Kawasaki 213-0012, Japan
[c] Near-Field Optics Group, Kanagawa Academy of Science and Technology, KSP East-409, 3-2-1 Sakado, Takatsu-ku, Kawasaki 213-0012, Japan
[d] Department of Electronics and Electrical Engineering, Faculty of Science and Technology, Keio University, 3-14-1 Hiyoshi, Kohoku-ku, Yokohama-shi, Kanagawa-ken 223-8522, Japan
[e] Institute of Medicinal Chemistry, Hoshi University, 2-4-41 Ebara, Shinagawa-ku, Tokyo 142-8501, Japan
[f] Medical Engineering Laboratory, Research Center for Medical Science, Jikei University School of Medicine, 3-25-8, Nishi-shinbashi, Minato-ku, Tokyo 105-8461 Japan

ARTICLE INFO

Article history:
Received 20 August 2010
Received in revised form 21 October 2010
Accepted 11 November 2010
Available online 18 November 2010

Keywords:
Polymeric micelle
Camptothecin
Incorporation
Inner core
Targeting
Morphology

ABSTRACT

We incorporated an anticancer agent, camptothecin (CPT), into polymeric micelle carriers by using two different solvents (TFE and chloroform) in the solvent-evaporation drug incorporation process. We observed significant differences in the drug-incorporation behaviors, in the morphologies of the incorporated drug and the polymeric micelles, and in the pharmacokinetic behaviors between the two solvents' cases. In particular, the CPT-incorporated polymeric micelles prepared with TFE as the incorporation solvent exhibited more stable circulation in blood than those prepared with chloroform. This contrast indicates a novel technological perspective regarding the drug incorporation into polymeric micelle carriers. Morphological analyses of the inner core have revealed the presence of the directed alignment of the CPT molecules and CPT crystals in the micelle inner core. This is the first report of the morphologies of the drug incorporated into the polymeric micelle inner cores. We believe these analyses are very important for further pharmaceutical developments of polymeric micelle drug-carrier systems.

1. Introduction

Polymeric micelles have attracted much attention as a nano-sized drug carrier in drug delivery systems (DDS) (Yokoyama, 2005; Aliabadi and Lavasanifar, 2006; Yokoyama, 2007). Polymeric micelles are macromolecular assemblies that, formed from block copolymers or graft copolymers, have a spherical inner core and an outer shell (Tuzar and Kratochvil, 1976,). Most typically, polymeric micelle drug carrier systems form from an AB type of block copolymer possessing a hydrophobic block and a hydrophilic block (Bader et al., 1984; Yokoyama et al., 1989). Hydrophobic drugs are physically incorporated into the micelles' hydrophobic inner cores by means of hydrophobic interactions (Kwon et al., 1994a; Yokoyama et al., 1994; Molavi et al., 2008; Shin et al., 2009). Owing to their advantages such as very small size in a range of 10–100 nm and high structural stability, polymeric micelle carriers have been actively applied to drug targeting (Yokoyama et al., 1991; Yokoyama, 2005; Aliabadi and Lavasanifar, 2006). In particular, polymeric micelle systems have achieved successful tumor targeting (Kwon et al., 1994b; Yokoyama et al., 1999; Nishiyama et al., 2003; Kawano et al., 2006) through the enhanced permeability and retention (EPR) effect (Matsumura and Maeda, 1986; Maeda et al., 1992), which enables nano-sized carriers to deliver anti-cancer drugs selectively to solid tumor sites. Presently, five clinical trials are underway for tumor targeting with polymeric micelle systems (Matsumura et al., 2004; Hamaguchi et al., 2005; Koizumi et al., 2006; Hamaguchi et al., 2007; Nakajima et al., 2008a,b).

Among the several types of nano-sized carrier systems including liposomes, nano-spheres, antibodies, and water-soluble synthetic polymers, the polymeric micelle has exhibited strong advantages in applications to hydrophobic low-molecular-weight drugs owing to the micelle's large drug-loading capacity and the micelle's ability to maintain the water solubility of the given carrier system. Previous studies of polymeric micelle drug-carrier systems have indicated that the stable incorporation of drugs into the hydrophobic inner cores is essential for successful in vivo targeting (Yokoyama et al., 1999; Yokoyama, 2005). If the stability is low, the drug is very rapidly released (within a range of only several minutes) from the carrier, resulting in unsuccessful targeting. Kwon et al. reported that extremely low diffusion constant

* Corresponding author. Tel.: +81 3 3433 1111x2336; fax: +81 3 3459 6005.
E-mail address: masajun2093ryo@jikei.ac.jp (M. Yokoyama).

0378-5173/$ – see front matter © 2010 Elsevier B.V. All rights reserved.
doi:10.1016/j.ijpharm.2010.11.016

values in a 10^{-19} to 10^{-20} cm^2/s order were necessary for stable drug incorporation because the size of micelle inner cores is very small, being approximately 10 nm in diameter (Forrest et al., 2006a,b). Yokoyama et al. reported that a slight change in the chemical structures of inner-core-forming hydrophobic polymer chains had substantial effects on incorporation stability (Yokoyama et al., 2004; Watanabe et al., 2006; Yamamoto et al., 2007). However, little is known about key factors for stable incorporation. Furthermore, physico-chemical characterizations of the incorporated drug molecules have never been conducted even though these characterizations would no double be useful both for the elucidation and the achievement of incorporation stability. These characterizations may concern, for example, types of drug distribution (uniformly distributed or localized at specific sites such as a boundary with an outer shell), aggregation status (the dispersed individual drug molecules or the aggregation of drug molecules into a cluster), and drug molecules' polarity (randomly directed drug molecules or molecules aligned to a specific direction owing to intermolecular interactions). Researchers have reported that two successful polymeric micelle systems physically incorporated drug molecules possessing planar chemical structures, doxorubicin (Yokoyama et al., 1991, 1999) and camptothecin (CPT) (Watanabe et al., 2006; Yamamoto et al., 2007). Doxorubicin possesses a planar anthracycline ring, and CPT molecules have a planar five-membered-ring structure. Planar molecules can exhibit strong polarity if they are aligned in one direction through their intermolecular associations. Therefore, the polarity of incorporated drug molecules is a candidate for determining factors that underlie stable incorporation.

In this paper, we carry out the first physico-chemical examination of the incorporated drug molecules inside micelle inner cores by means of fluorescence spectroscopy and AFM. Furthermore, we evaluate effects that solvents used in drug-incorporation procedures can have on both the morphologies of inner cores and the morphologies of micelle structures. Then, we compare two polymeric micelle formulations that are different from each other only in the solvent used in the drug incorporation process, while the other factors, drug molecules and block copolymer structures, are the same between the two formulations. We observed a substantial difference in pharmacokinetic behaviors. This indicates that solvents can be an important factor in successful drug incorporation through the control of morphologies, whether in relation to incorporated drugs or polymeric micelles.

2. Materials and methods

2.1. Materials

(*S*)-(+)-Camptothecin and 1,1,1-trifluoro-2-propanol were purchased from Sigma-Aldrich (Tokyo branch, Japan) and were used as received. Reagent-grade solvents, chloroform, 2,2,2-trifluoroethanol (TFE), tetrahydrofuran (THF), dimethylsulfoxide (DMSO), N,N-dimethylformamide (DMF), N,N-dimethylacetamide (DMAc), 1,4-dioxane, 1,1,1,3,3,3-hexafluoro isopropanol were purchased from Wako Chemicals (Tokyo, Japan) and were used as received. Poly(ethylene glycol)-b-poly(aspartic acid-co-benzyl aspartate) (PEG-P(Asp(Bzl 74))) was synthesized as previously reported (Opanasopit et al., 2004; Yokoyama et al., 2004; Yamamoto et al., 2007), and its chemical structure is shown in Fig. 1. The average molecular weight of PEG was 5200 (n = 118 in Fig. 1), and the average number of Asp units (m) was 27. The current study converted 74% of the aspartic-acid units into benzyl-aspartate units through an esterification reaction of poly(ethylene glycol)-b-poly(aspartic acid). Our group has investigated variations of this type of block polymer by, for example, changing the percentage of benzyl aspartate units or using hydrophobic ester groups

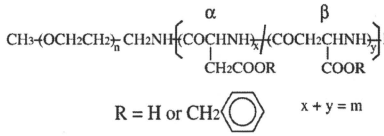

Fig. 1. Chemical structure of a block copolymer for micelle carriers.

other than benzyl ester, and so far PEG-P(Asp(Bzl 74) has worked well for our efforts to incorporate camptothecin into polymeric micelles (Yokoyama et al., 2004; Yamamoto et al., 2007) and to incorporate retinoids into polymeric micelles (Chansri et al., 2008; Okuda et al., 2008, 2009). The aspartate amide bond can be either α or β, and our group previously had reported that PEG-P(Asp(Bzl)) with all α aspartate amide bonds did not result in the formation of stable CPT-incorporated micelles. Therefore, in the current study, we used a polymer that has the aspartate amide bond with an α/β ratio of 1/3.

In some measurements, block copolymers possessing the same chain lengths and similar benzyl-esterification degrees (70% and 82%) were used.

2.2. Preparation of camptothecin-incorporated polymeric micelles

Camptothecin (CPT)-incorporated polymeric micelles were prepared through a solvent evaporation method (Yokoyama et al., 2004; Watanabe et al., 2006). In this method, 5 mg of PEG-P(Asp(Bzl 74)) and an appropriate amount of 1 mg/mL CPT solution (in TFE or chloroform) were mixed in a 9 mL glass vial, followed by evaporation of the solvent under a dry nitrogen-gas flow with stirring at 40–50 °C. After complete evaporation, a dried film was obtained. To this film was added 4 mL of water, and the mixture was sonicated with a probe type ultrasonication instrument (VCX-750 equipped with a 5 mm tapered micro tip, Sonics & Materials, Newtown, CT, USA). For removal of possible precipitates and large particles, the obtained solution was centrifuged at 10,000 rpm (12,000 × g) for 10 min by the use of a centrifuge Himac CR21G equipped with an R20A2 rotor (Hitachi Koki Co., Ltd., Tokyo, Japan) at 20 °C, and then was filtered through a 0.45 μm Millex-HV PVDF filter (Millipore Corp., Billerica, MA, USA), resulting in an aqueous solution of CPT-incorporated polymeric micelles. Polymeric micelles prepared by the use of TFE are denoted as "micelle A", and those prepared by the use of chloroform as "micelle B". A blank experiment was conducted in the absence of the block copolymer for estimating the amount of free CPT that would not be incorporated into polymeric micelles but that would be included in the solution. As the blank controls in which no polymer was used, CPT in a 1 mg/mL solution was added to an empty vial so that the total mass of CPT would be 0.5, 1.0, 2.0, or 5.0 mg, corresponding to 10, 20, 40, or 100 wt.% CPT with respect to polymers if they were present. The solvent was removed by evaporation, followed by an addition of water, sonication, centrifugation, and filtration according to the same approach as that adopted in the preparation of the CPT micelle solution. The concentration of CPT was measured with a UV–vis spectrometer. The procedure for UV–vis measurements is described in the UV–-vis spectroscopy Section 2.3.2.

2.3. Measurements

2.3.1. Dynamic light scattering (DLS)

Particle sizes of micelles were measured with a dynamic light scattering (DLS) instrument DLS-7000 (Otsuka Electronics, Tokyo,

Japan). The DLS samples were prepared by dilution of the micelle solutions with filtered Millipore water, while the polymer concentration was kept above the critical micelle concentration (CMC) reported in our previous paper (Yamamoto et al., 2007). The measurements were made at 25 °C, and scattering was observed at a 90° angle with respect to the incident beam. The Cumulant average particle size and particle size distribution from a non-negative least square method were determined by the use of software provided with the instrument. The DLS sample concentration was adjusted so that the scattering intensity would be within the measurable range, while the polymer concentration would be above its CMC.

2.3.2. UV–vis spectroscopy

The CPT concentrations of the micelle solutions were determined with a UV–vis spectrometer (Jasco V-550, JASCO Corp., Tokyo, Japan). The path length of the quartz cell was 1 cm. The scan range was 250–600 nm; the band width was set at 0.5 nm. CPT concentrations were calculated from an equation obtained from a calibration plot. Typically, a 150 μL sample aqueous solution, 150 μL water, and 2.7 mL DMSO were mixed to provide a 9:1 (vol./vol.) mixture of DMSO and water, and the peak top absorbance at 365 nm (A365) and the absorbance at 600 nm (A600) were recorded. The subtracted values (A365–A600) were used for the [CPT] determination. The CPT recovery in the drug-incorporation procedure was calculated through division of the micelle solution's "CPT amount" by the feed-added "CPT amount". When water was used in relation to the DMSO-water mixture as the solvent for UV–vis measurements, the dilution was 1/10 instead of 1/20.

We investigated the solubility of CPT in several organic solvents such as THF, DMF, and 1,4-dioxane, as well as in fluorinated solvents such as TFE and 1,1,1,3,3,3-hexafluoro isopropanol. CPT was dissolved in each solvent (up to 5 mg/mL), and absorbance at 600 nm was measured with a UV–vis spectrometer. We estimated the solubility of CPT in each solvent by measuring turbidity at 600 nm, because the CPT molecule has no absorption at 600 nm, and thus the absorbance recorded at this wavelength is caused by the light scattering of aggregated CPT.

2.3.3. Fluorescence spectroscopy

We measured polarization degrees of CPT molecules in the polymeric micelles by using a fluorescence-spectroscopy instrument (Jasco FP-6500, JASCO Corp., Tokyo, Japan) equipped with a polarization unit (JASCO Corp., Tokyo, Japan). Fluorescent spectra were recorded with excitation and emission at 351.5 nm and 433.0 nm, respectively. Band widths of excitation and emission were set at 10 nm and 3 nm, respectively. A fluorescence anisotropy (r) value was obtained by the formula $r = (I_{vv} - G \times I_{vh})/(I_{vv} + G \times I_{vh})$, where G is equivalent to I_{hv}/I_{hh}, where I_{vv} is equivalent to fluorescence intensity at vertical (excitation, Ex) and vertical (emission, Em) positions, where I_{vh} is equivalent to fluorescence intensity at vertical (Ex) and horizontal (Em) positions, where I_{hv} is equivalent to fluorescence intensity at horizontal (Ex) and vertical (Em) positions, and where I_{hh} is equivalent to fluorescence intensity at horizontal (Ex) and horizontal (Em) positions.

2.3.4. Polarized fluorescence microscopy

Polarized fluorescence microscopy, featuring a hand-made microscope, was carried out for a dried polymeric micelle sample on a quartz plate. An Ar-ion laser (351.1 nm; Innova 300, Coherent Inc., California, U.S.A.) with a polarization controller (SIGMA KOKI, Tokyo, Japan) was used for excitation, and a perpendicularly polarized component of the fluorescence signal was selectively observed with a supersensitive CCD camera (C4742-95ER, Hamamatsu Photonics, Shizuoka, Japan).

2.3.5. Atomic force microscopy (AFM)

For imaging by atomic force microscopy (AFM), micellar solutions were deposited on freshly cleaved mica, rinsed with water after a few minutes, and air (or nitrogen) dried; in this way, films were obtained. Height-contrast and phase-contrast images were obtained in air with an atomic force microscope MFP-3D (Asylum Research, Santa Barbara, CA, USA) in AC mode.

2.3.6. Determination of CPT concentrations in plasma

A CPT micelle solution in 0.9 wt.% NaCl was administered via the tail vein to male ddY mice (5 weeks old) at 2.5 mg CPT/kg. At 4 h after injection, blood was collected with a heparinized syringe, and the collected blood sample was centrifuged so that plasma could be obtained. The plasma was acidified with a 0.15 M phosphoric acid aqueous solution, and CPT was extracted with 4/1 (vol./vol.) chloroform/methanol. The extracted CPT was analyzed by the use of an HPLC system (LC-10AT, Shimadzu Corp., Kyoto, Japan) equipped with a Tosoh TSK-gel ODS-80Ts column (Tosoh, Corp., Tokyo, Japan), and a fluorescence detector set at λ_{ex} = 369 nm and λ_{em} = 426 nm. The mobile phase was a 23/77 vol./vol. mixture of acetonitrile/triethylamine acetate buffer (1.0% vol./vol., pH 5.5), and the flow rate of 1.0 mL/min was used.

2.3.7. Calculation of cohesion parameters

The partial cohesion parameters (δD, δP, and δH) for CPT and polymers were calculated from the molar volumes and the Hansen parameters listed in a reference (Hansen, C.M., 2007), and the total (Hildebrand) cohesion (solubility) parameter δt was obtained with the equation $\delta t = (\delta D^2 + \delta P^2 + \delta H^2)^{1/2}$. The parameters for the hydrophobic block, P(Asp(Bzl 74)), were calculated as molar-ratio-averages of the two repeating units Asp (26%) and Asp(Bzl) (74%).

3. Results

3.1. Preparation of CPT-incorporated polymeric micelles

We used block copolymer PEG-P(Asp(Bzl 74)) for the incorporation of camptothecin (CPT) into the polymeric micelle. Our method for the drug incorporation into the micelles proceeded in two steps: solvent evaporation and sonication. We will denote micelles prepared by evaporation of TFE as "micelle A", and those prepared by evaporation of chloroform as "micelle B". Among them, samples containing different amounts of CPT were prepared, and they will be represented by how much wt.% CPT/polymer was used in the feed, i.e., 10% CPT, 20% CPT, and so on. Except for the solvent used in the film preparation, all other process factors were identical between micelles A and B. We varied the CPT/polymer ratio between 5 and 100% by weight, by adding an appropriate volume of 1 mg/mL CPT solution. Therefore, the total volume of the solvent was different for each sample, depending on the amount of CPT required.

3.2. Solubility of CPT in various solvents

We evaluated solubility of CPT in several organic solvents. We present the results with TFE, chloroform, and DMSO in Fig. 2 and omit other solvents for presentation clarity. In chloroform, the measured absorbance was similar to that in THF or DMSO up to 1 mg/mL, but it took a sudden jump at this concentration and went out of scale for [CPT] > 1 mg/mL. The solubility of CPT in THF and 1,4-dioxane was also poor as these solvents also gave high absorbance at 600 nm for even [CPT] < 1 mg/mL, and CPT was practically insoluble at the higher concentrations. On the other hand, CPT was well dissolved in TFE, DMSO, DMF, and DMAc. CPT was moderately soluble in 1,1,1-trifluoro-2-propanol and 1,1,1,3,3,3-hexafluoro isopropanol but not as soluble as TFE. From these results we concluded that

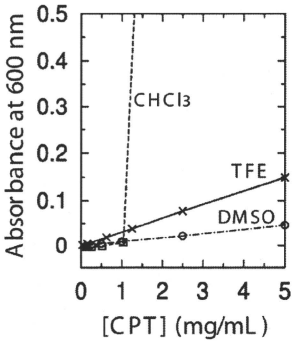

Fig. 2. Turbidity of CPT solutions in DMSO (○), TFE (×), and chloroform (□) as measured with a UV-VIS spectrometer.

the CPT solution used to prepare micelles should be in TFE or chloroform, and that [CPT] ≤1 mg/mL. One might consider the use of DMSO; however in our evaporation method, the solvent needs to be removed from the system. Therefore, solvents with a high boiling point are not preferred (b.p. DMSO = 189 °C, chloroform = 61 °C).

3.3. Characterization of CPT-incorporated micelles

3.3.1. Particle size determination by dynamic light scattering (DLS)

Fig. 3(a) shows the average Cumulant diameter of CPT micelles for various CPT amounts in the feed (5–100 wt.% with respect to polymers) as measured by DLS. The Cumulant average particle size ranged from ~80 to ~160 nm both for micelle A (prepared from TFE) and micelle B (prepared from CHCl3). The particle size of micelle B appeared to reach a limiting value of ~160 nm for a CPT/polymer weight ratio greater than 20%, whereas that of micelle A reached the first plateau between 20 and 40 wt.% CPT at ~110 nm, and then continued to increase to ~160 nm, reaching the second plateau between 40 and 60 wt.% CPT. Overall, the general tendency was that the particle size increased with the amount of CPT employed.

Fig. 4 shows the weight-weighted particle-size distribution of micelles prepared from 10 wt.% CPT/polymer as representative data. In Fig. 4(a), micelle A was observed to possess two peaks at 32 nm and 130 nm. Similarly, Fig. 4(b) corresponding to micelle B shows 2 peaks: one at 48 nm and the other at 168 nm, indicating that the aqueous micellar solutions contained two populations of particles. We assumed that the latter was a secondary association of micelles. In both of the micelle samples, the group of smaller particles constituted the majority (89% and 86% in weight for micelle A and micelle B, respectively) in the two populations.

3.3.2. CPT recovery in preparation of CPT-incorporated micelles

Fig. 3(b) shows CPT concentrations recovered in 4 mL of polymeric micelle aqueous solutions after the product was purified through centrifugation and filtration, plotted against the weight % of CPT/polymer in the feed. The same behaviors were observed between the average diameters shown in Fig. 3(a) and the CPT concentrations shown in Fig. 3(b) for both micelle A and micelle B. The CPT concentration in micelle B reached a plateau of ~20 wt.% CPT/polymer in the feed, where the maximum [CPT] value was ~80 μg/mL. This behavior was identical to the behavior of the Cumulant diameter shown in Fig. 3(a). Micelle A reached two

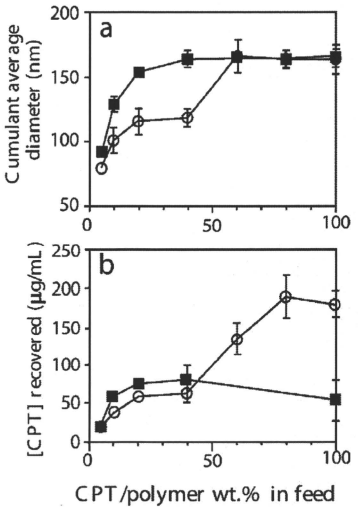

Fig. 3. CPT incorporation behaviors of polymeric micelles. (a) Cumulant average diameter of CPT micelles prepared with TFE(○, micelle A) or chloroform (■, micelle B). Data are shown in the average ± standard deviation of three measurements of the Cumulant average. (b) The CPT concentration recovered in an aqueous CPT micelle solution. Preparations of the micelles rested on TFE (○, micelle A) or chloroform (■, micelle B). Data are shown in the average ± standard deviation of three measurements.

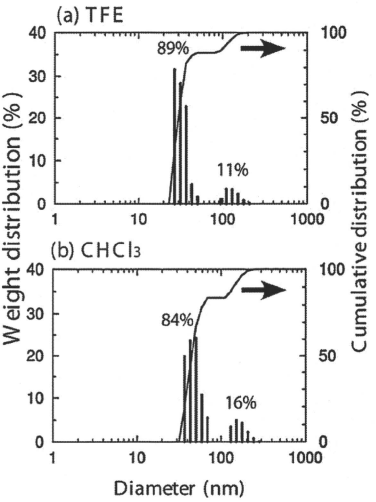

Fig. 4. Weight-weighted diameter distributions measured by dynamic light scattering for (a) micelle A (prepared from a solution in TFE) and (b) micelle B (prepared from a solution in chloroform). The CPT/polymer wt. ratio in the feed was 10% for the two cases. Values (%) shown in figures are weight proportions of the two peaks.

Table 1
CPT concentrations recovered after each step.

Solvent	CPT amounts in the feed[a]		[CPT] μg/mL after each step					
			Sonication→		Centrifugation→		Filtration	
TFE	0.5 mg	10 wt.%	120 ± 13	110	38 ± 5	31	5± 5	27
	2.0 mg	40 wt.%	470 ± 13	490	71 ±45	95	17 ±10	86
	5.0 mg	100 wt.%	I 1030 ±110	1100	66 ±10	170	27 ±12	160
CHCl3	0.5 mg	10 wt.%	89±23	140	8± 3	27	3± 0	27
	2.0 mg	40 wt.%	400 ± 44	560	18 ± 4	26	3± 1	25
	5.0 mg	100 wt.%	730 ± 24	1200	29 ±22	24	2± 1	23

Values at the left hand side are obtained without polymer and shown with the average ± S.D. ($n = 3$). Values at the right hand side are obtained with polymer ($n = 1$).
[a] CPT amounts are shown by weight for "without polymer" cases, and by CPT/polymer weight ratio in the feed for "with polymer" cases.

plateaus: the first one around 50 μg/mL at 20 wt.% CPT, and the second plateau around 190 μg/mL at 80 wt.% CPT. This was also the same behavior of the recovered CPT concentration shown in Fig. 3(a). In terms of efficiency (amount of CPT recovered/amount of CPT used), for micelle A, CPT was most efficiently recovered between levels of 5 and 10 wt.% CPT/polymer (~30% recovery), and efficiency of CPT recovery dropped to ~15% around 40 wt.% CPT, and then slightly improved in the 60–80 wt.% CPT range, and finally settled ~15% at 100 wt.% CPT/polymer. For micelle B, CPT recovery was highest at 10 wt.% CPT where ~45% of CPT used was recovered in the product, and then the efficiency of CPT recovery decreased steadily with the amount of CPT used. The lowest value in the range we examined in this study was only ~5% at 100 wt.% CPT. We treat the drop in the CPT recovery efficiency as a result of the precipitation of unincorporated CPT, as described below.

A series of experiments were conducted for estimation of the amount of unincorporated CPT. Concentrations of CPT in aqueous solutions were measured with a UV spectrometer after each step of the preparation procedure, namely, (1) the sonication step, (2) the centrifugation step, and (3) the filtration step. In these experiments, the procedure used for the CPT micelle preparation was carried out with and without the polymer. Table 1 summarizes results. The amount of CPT 0.5, 1.0, 2.0, or 5.0 mg in "without polymer" cases corresponded to 10, 20, 40, or 100% CPT/polymer ratios in "with polymer" cases. After the sonication step, considerably high amounts of CPT (ca. 60–100%) were recovered in both "with polymer" and "without polymer" cases, as revealed by the large values in Table 1's sonication columns. For "without polymer" cases, most of the recovered CPT seemed to be present as dispersion of small insoluble aggregates because the obtained solutions were turbid. Therefore, after the centrifugation step, the recovered CPT concentrations substantially dropped to 8–29 μg/mL for CHCl3 solvent cases and 38–71 μg/mL for TFE solvent cases owing to precipitation of the insoluble aggregates. In contrast, for "with polymer" cases, the recovered CPT amounts exhibited little change through the filtration step, while a considerable drop was observed in the "without polymer" cases after the filtration step possibly because of adsorption of the insoluble aggregates on a filter membrane

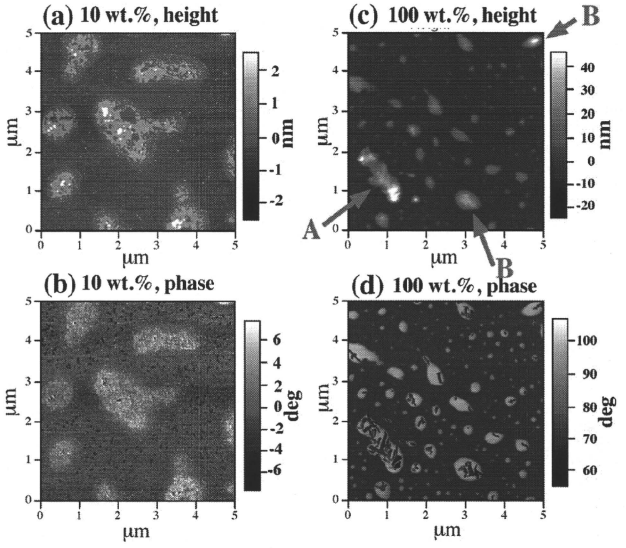

Fig. 5. AFM images of micelle A (prepared from a solution in TFE). The CPT/polymer wt.% in the feed was either 10% (a and b) or 100% (c and d). Images (a) and (c) are of height, while (b) and (d) concern phases.

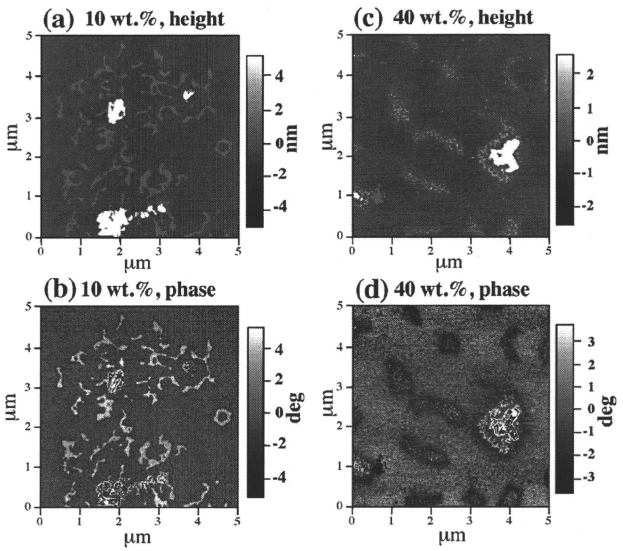

Fig. 6. AFM images of micelle B (prepared from a solution in chloroform). The CPT/polymer wt.% in the feed was either 10% (a and b) or 40% (c and d). Images (a) and (c) are of height, while (b) and (d) concern phases.

through hydrophobic interactions. These results indicate that most of the recovered CPT in the micelle solutions was incorporated into the polymeric micelles, and that low efficiency of the CPT incorporation at high CPT-polymer ratios resulted from the presence of large amounts of unincorporated CPT.

3.3.3. *Morphological observation of CPT-incorporated polymeric micelles by AFM*

AFM images of micelles are shown in Figs. 5 and 6. We obtained images by using dried films: aqueous micelle solutions were deposited on mica, and then the mica surfaces were rinsed with Millipore water for removal of excess sample, and finally dry nitrogen gas served to dry the surfaces. These dried films may not represent the real status of micelles in solution, but still provide useful topographical information on the samples.

A 5 μm × 5 μm scan of a film prepared from micelle A (10 wt.% CPT/polymer) shows patches of high contrast areas (Fig. 5, both height (a) and phase (b) images). The patches varied in size, but most of them occupied several hundred nm by several hundred nm to a few microns of area. The patches were relatively flat areas surrounded by small round-shaped islands less than 30 nm in diameter. Some islands were found also within patches; these spots were ~5–20 nm tall with respect to the surrounding flat area, whereas the flat area was <5 nm high with respect to the lowest part of the sample. In these images, we could not assign polymer locations or CPT locations.

Interesting images were observed in a film of micelle A prepared from a 100 wt.% CPT/polymer ratio (Fig. 5(c) and (d)). In the height image (Fig. 5(c)), round objects of various sizes ranging from ~10 nm to several hundred nm in diameter were present, along with larger elliptical objects. The cross-section of this image showed that the height difference between the dark area and the top of the largest island (pointed at with arrow A) was approximately 30 nm. In some other areas, smaller objects with brighter contrast were observed (pointed at with arrow B), indicating the existence of a different species from that of the round area. In the corresponding phase image (Fig. 5(d)), round objects in bright contrast were found at the same positions and in the same sizes as those in the height image, and in addition to these islands were observed rectangular objects of dark contrast on top of those islands. Judging from this image's phase intensity (gray scale bar on the side), the hardness of the rectangular areas was similar to that of the background (most likely bare mica, possible with some polymer coating), while the bright area was softer than the dark areas. We believe that the bright areas represent the polymer, and the dark rectangular areas represent the crystals of CPT. These crystal-like rods were ~0.1 μm × 1 μm or smaller, and were positioned on top of the polymer islands.

Fig. 6 shows AFM images of micelle B prepared from either 10 wt.% (a,b) CPT/polymer or 40 wt.% (c,d) CPT/polymer in the feed. Fig. 6(a) represents a height image obtained from micelle B prepared at a 10 wt.% CPT/polymer ratio. In this 5 μm × 5 μm image, the sample appears to have two distinct areas: string-like structures that are <5 nm tall with respect to the lowest point of the substrate, and areas of much higher contrast, ~50 nm tall with respect to the surrounding area. In the phase image, the latter structure seems to be a collection of smaller lumps whose contrast differs from the string-like structures. When the height contrast was optimized for these tall lumps (image not shown here), the rectangular rods were the same shape as that of the crystal-like structure in Fig. 5(d). Although these AFM measurements with the dried films may cause artifacts in the film preparation process, these results suggest two matters. One, CPT molecules formed crystals in a high CPR/polymer feed ratio. Second, empty (incorporating no

CPT molecules) polymeric micelles may be present more probably in a high CPR/polymer feed ratio.

Fig. 6(c) and (d) were obtained from micelle B prepared in CPT/polymer 40 wt.%. These images were similar to Fig. 5(a) and (b) obtained from micelle A prepared from 10 wt.% CPT/polymer in TFE. The patches that were <5 nm in height with respect to the lowest part of the substrate were ubiquitous and were similar to those of micelle A; however, in addition to these patches, rod-like structures of ~10–40 nm thickness compared to the surroundings were found. These rod-like objects were the same as those seen in Fig. 6(a) and (b). These results suggest that aggregation of CPT molecules occurred in micelle B in a more drastic manner than micelle A, and that the empty micelles were present in micelle B in a higher proportion than micelle A.

3.3.4. *CPT in micelle solutions monitored by UV–vis spectroscopy*

As described earlier, the amount of CPT contained in a micelle solution was determined in a mixture of DMSO and water (9:1, vol./vol.) by UV–vis spectroscopy. This mixed solvent dissolves both CPT and the hydrophobic block of the copolymer. Therefore, CPT molecules that were released from the polymeric micelles were measured in this mixed solvent. For such a measurement only the peak intensity was necessary, but we now turn to the spectrum itself measured in water to examine the environment that surrounds CPT. Fig. 7 shows UV spectra of aqueous CPT-incorporated micelle solutions prepared at various CPT/polymer ratios by the use of (a) TFE and (b) chloroform as a solvent in the micelle preparation. CPT micelle solutions were diluted to a 1/10 concentration in water, corresponding to a CPT concentration of ~2–20 μg/mL and corresponding to a polymer concentration of ~0.1 mg/mL that was much higher than polymer's critical micelle concentration (Yamamoto et al., 2007). The spectra were normalized at a peak intensity of 351.5 nm. There were two main peaks in the spectra, as shown in Fig. 7: 351.5 nm and 367.5 nm. The shoulder peak around 395 nm, which was prominent in 60–100 wt.% CPT/polymer in micelle A, suggests intermolecular association of CPT molecules. The same shoulder was also observed in micelle B for a CPT/polymer wt.% range of 20–100%, but to a lesser degree than micelle A. The hypochromic effect was also observed at 367.5 nm, where the peak intensity decreased for some of the samples, compared with that of 5% CPT/polymer samples. This also indicates the intermolecular association of CPTs' aromatic chromophores.

3.3.5. *Polarization degree of CPT molecules in the polymeric micelles*

We evaluated the polarization degree of CPT molecules in the polymeric micelles by measuring the fluorescence anisotropy value (r). Fig. 8 shows the fluorescence anisotropy of CPT molecules in various CPT concentrations. The polarization degree reflects environments of incorporated CPT molecules. For polymeric micelle samples PEG-P(Asp(Bzl 70)) and PEG-P(Asp(Bzl 82)), the concentration of polymer was constant at 1.67 mg/mL, while CPT concentrations were varied through adjustments of CPT quantity used in the incorporation procedure into the micelles. Two influencing factors are present for the polarization degree; mobility/rigidity of environments where fluorescence molecules are present, and fluorescence extinction by the other fluorescence molecules. A greater polarization degree is observed for the fluorescence molecules in the more rigid (=less mobile) environments, while the polarization degree can change (raised or lowered) through the extinction by the other fluorescence molecules. Usually, the mobility/rigidity is the determining factor for the polarization degree of molecules incorporated in polymeric micelle inner cores, since it is obvious that the CPT molecules incorporated into the micelle inner core exist in a more rigid environment than the one where free CPT molecules dissolved in DMSO. (DMSO

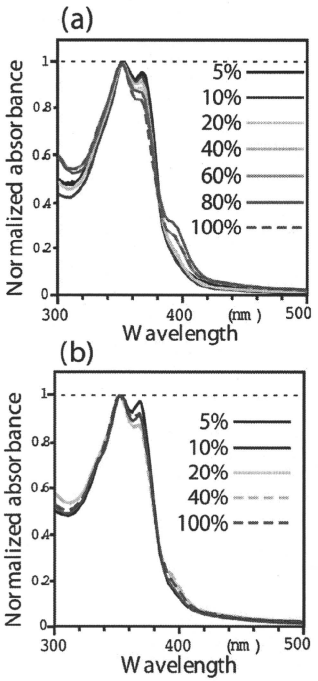

Fig. 7. Normalized UV spectra of CPT-incorporated micelles in aqueous solutions: (a) micelle A (prepared from a solution in TFE), and (b) micelle B (prepared from a solution in chloroform). The percentages shown in figures indicate the CPT/polymer wt.% in the feed.

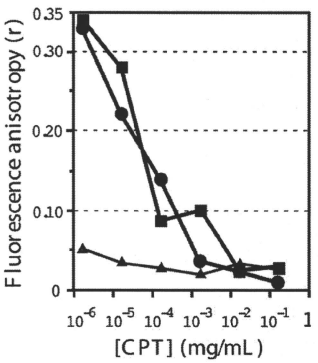

Fig. 8. Polarization degree of CPT fluorescence. CPT in polymeric micelles forming from PEG-P(Asp(Bzl 70): ●, in polymeric micelles forming from PEG-P(Asp(Bzl 82): ■, and CPT just dissolved in DMSO: ▲.

is a good solvent as proven in Fig. 2.) Unexpectedly, for these two polymeric micelle samples, the CPT polarization degrees were almost the same as or lower than the polarization degrees of free (unincorporated) CPT molecules dissolved in DMSO at high CPT concentrations of 1.7×10^{-1} and 1.7×10^{-2} mg/mL. This indicates that the fluorescence extinction was the determining factor in this CPT concentration range in a different manner from the usual polymeric micelle cases where the mobility/rigidity is the determining factor. In fact, the polarization degrees of the polymeric micelle samples were observed to become greater as the CPT concentration was lowered, while the polarization degrees were almost constant for the free CPT solution in DMSO in the whole measurement range. This tells two matters. One, the rigid micelle inner core environment was confirmed, as already reported with a dipyrene fluorescence probe (Yamamoto et al., 2007). Second, the polarization of CPT molecules can be detected, but only in much lower CPT concentration ranges than those used in actual formulations for in vitro and in vivo evaluations where a high CPT content (ca. 1–40 CPT wt. %) is preferably applied. Irrespective of this gap in the CPT concentration range, these results are the first information concerning drug molecule's incorporation status in the polymeric micelle inner core. By referring to this fact, we carried out the following polarized fluorescence microscopy measurements in this low CPT concentration range as described in the next section.

3.3.6. *Polarized fluorescence microscopy*

In order to detect the polarized fluorescence of CPT molecules, we carried out polarized fluorescence microscopy measurements on a quartz plate with a dried micelle sample having a low CPT/polymer ratio (0.001%, which corresponds to the micelle prepared at 1.7×10^{-5} mg/kg [CPT] in Fig. 8). At the emission side, the perpendicularly polarized component of the fluorescence signal was selectively observed with a supersensitive CCD camera, while at the excitation side an Ar-ion laser was applied with a polarization controller. As shown in Fig. 9, two bright spots were observed in this area, and fluorescence intensities of these two spots were found to change in accordance with the polarization controller angle. For spots A and B, both the brightest and darkest signals appeared with exactly 180° intervals. Therefore, it was revealed that this measurement detected the polarized fluorescence of the CPT molecules. This is the first direct visualization of the polarity of the drug molecules incorporated in polymeric micelles. Bright spots were not observed at higher CPT/polymer ratios (0.1%, 1%, and 10%, data not shown) owing to the florescence extinction observed in the polarized fluorescence spectra shown in Fig. 8. Therefore, this method could not reveal morphologies of the CPT molecules at the high CPT/polymer ratios that were used for in vitro and in vivo evaluations. The fluorescence extinction behaviors are dependent on excitation/emission characteristics of molecules; therefore, this method may be applied to drug molecules exhibiting prominent extinction behaviors. This polarized fluorescence technique can be a powerful and direct method to analyze morphologies of drug molecules in the micelle inner core.

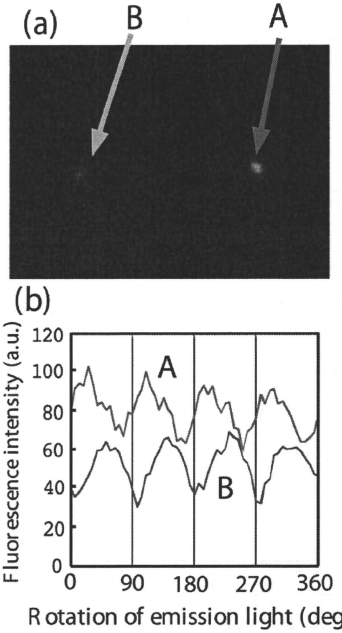

Fig. 9. Polarization fluorescence microscopic image (a) and its intensity change relative to the rotation of polarized emission light (b).

3.4. *Determination of CPT concentrations in plasma*

In Table 2, we summarize results of CPT concentrations in plasma at 4 h after intravenous injection of the CPT-incorporated polymeric micelles. We previously examined time course profiles in blood of [CPT] in polymeric micelles, and reported that CPT micelles prepared from PEG-P(Asp(Bzl 75)) exhibited the best in vivo stability value (9.3% dose) among similar polymers of various percentages of benzyl groups attached at the hydroxyl groups of P(Asp) (Watanabe et al., 2006). In this Table, we compare the values obtained from this previous report with our new results. In the previous method, CPT was incorporated by the use of chloroform as the evaporation solvent. We also observed that the CPT/polymer ratio did not affect so much (7.6 and 5.3% doses) the CPT concentrations in blood when we were using PEG-P(Asp(Bzl 57)), and

Table 2
CPT concentrations in blood 4 h after intravenous injection of polymeric micelles.

polymer	CPT/polymer wt. ratio in feed	solvent used for incorporation	CPT in blood (% dose)	reference
PEG-P(Asp(Bzl 74))	10%	TFE	27.3 ± 2.6	
PEG-P(Asp(Bzl 74))	5%	TFE	28.6 ± 0.5	
PEG-P(Asp(Bzl 75))	40%	Chloroform	9.3 ± 1.8	Watanabe et al., 2006
PEG-P(Asp(Bzl 57))	40%	Chloroform	7.6 ± 0.8	
PEG-P(Asp(Bzl 57))	10%	Chloroform	5.3 ± 0.6	

Table 3
Cohesion parameters of CPT, solvents, and an inner-core-forming polymer block.

	δD	δP	δH	δt
CPT	25.8	6.8	8.9	28.1
TFE	15.4	8.3	16.4	24.0
chloroform	17.8	3.1	5.7	18.9
DMSO	18.4	16.4	10.2	26.7
P(Asp) block	23.2	22.2	13.4	34.8
P(Asp (Bzl 74)) block	24.9	10.4	8.1	28.2

δD: dispersion solubility parameter.δP: Polar solubility parameter.δH: hydrogen bonding solubility parameter.δt: total (hildebrand) solubility parameter; $\delta t = (\delta D^2 + \delta P^2 + \delta H^2)^{1/2}$.Parameters are calculated according to methods and values of a reference (Hansen, 2007 Parameters of TFE, chloroform, and DMSO were taken from the reference. The units are: $(J\,cm^{-3})^{1/2}$.

that the CPT concentration did not exceed a 10% dose for the CPT-incorporated micelles prepared with chloroform. In contrast, with the polymeric micelles prepared from TFE, we obtained significantly higher CPT concentrations around the 28% dose. When we varied the CPT/polymer levels between 5% and 10%, no change in the CPT concentrations was observed. All these results indicate that the choice of organic solvent is an important key to obtaining the stable circulation of incorporated drugs in blood.

4. Discussion

In polymeric micelle research for drug delivery systems, most efforts have been made in carrier polymer design and preferable choice of the carrier polymer-drug combinations for the targetable carrier systems. The drug-incorporation process may be a very important step in preparing various polymeric micelle drug carrier systems; however, examinations of the topic are scarce. In this paper, we reported that the solvent used for the drug-incorporation process into polymeric micelles had substantial effects on drug-incorporation efficiency, micelle diameter, morphologies of the micelles and of the incorporated drug, and in vivo pharmacokinetic behavior of the incorporated drug. In particular, considerable prolongation of circulation in the bloodstream, which is essential for passive tumor targeting, was successfully obtained by the choice of an appropriate organic solvent used in the evaporation-"drug incorporation" method. As far as we know, this is the first indication of the solvent's importance for the prolongation of circulation in blood of polymeric micelle targeting systems.

When we used 2,2,2-trifluoroethanol (TFE) for the incorporation solvent, we obtained smaller average diameters of the micelles (in a drug/polymer ratio range from 5 wt.% to 40 wt.%) and more stable circulation in blood than the micelles did when prepared by the use of chloroform as the incorporation solvent. We think that the higher CPT solubility of TFE at CPT concentrations higher than 1 mg/mL is the reason for the preferable micelle formulation that exhibited the more stable circulation in blood than that of the chloroform case. Here, we conducted solubility and miscibility estimations by calculating solubility parameters. Table 3 lists the cohesion parameters of the materials: CPT, the solvents used in our experiment, and the hydrophobic block of the polymer. Theoretically, the smaller the difference between the δt of the drug and the solvent, the more soluble the drug is in the solvent (Huynh et al., 2008). If that is the case, the solubility of the three solvents' CPT is, from greater to smaller, DMSO > TFE > chloroform. This is in agreement with the results obtained from the turbidity experiment. Furthermore, the cohesion parameters of CPT are quite similar to those of the P(Asp(Bzl 74)) block of the polymer. This block copolymer PEG-P(Asp(Bzl 74) has been chosen from among several compositions and other hydrophobic moiety structures in terms of stable drug incorporation of CPT (Yokoyama et al., 2004; Yamamoto et al., 2007). Therefore, the calculated value agrees well with this fact. It is expected that the drug incorporation into the micelle inner core is of higher efficiency and is more stable when the drug is more miscible with the inner core-forming hydrophobic polymer block. However, more examinations with various combinations of the drug and the inner core-forming block are required for valuable applications of solubility-parameter calculations to reliable estimations of the optimized combination of a given drug and with a given carrier polymer.

We consider that the TFE's higher solubility of CPT efficiently inhibits large aggregates' formation of CPT molecules, resulting in higher CPT-incorporation yields and in the smaller micelle diameters than is the case with chloroform. AFM images in Fig. 6 indicate the presence of many empty micelles that do not contain CPT. This can be because large CPT aggregates formed aggressively during the solvent evaporation of chloroform, resulting in a large amount of unincorporated CPT aggregates.

As discussed above, this paper presents a novel methodology in polymeric micelle carrier systems for better formulations regarding the choice of an appropriate solvent in the evaporation drug-incorporation process. This is a very simple approach, but is no less important for being simple because the choice considerably changed pharmacokinetic behavior, as demonstrated in Table 3.

In addition to the importance of the solvent choice, this paper provided the first morphological information on incorporated drugs in polymeric micelles' inner cores. In general, morphological analyses of incorporated drugs are very difficult owing to the very small size of micelle inner cores (several nm). In this paper, we have shown the presence of the polarized CPT molecules in the inner cores by measuring fluorescence polarization spectra and microscopic images, as well as by measuring the formation of CPT crystals through AFM observations. We believe these morphological factors are very important for optimized drug incorporation into the polymeric micelle carriers although technical difficulties prevented us from identifying direct morphological evidence for stable CPT incorporation in the TFE case.

5. Conclusion

We observed substantial effects that solvents used in drug-incorporation processes can have on drug-incorporation behaviors, on the morphologies of both the incorporated drug and the polymeric micelles, and on pharmacokinetic behaviors. Simply through an appropriate choice of solvent, the circulation of an incorporated drug in blood was greatly improved for tumor targeting. Morphological analyses of the inner core revealed the directed alignment of the CPT molecules and CPT crystals in the micelle inner core at a low and high CPT/polymer ratio, respectively. These analyses are important for further developments of polymeric micelle drug-carrier systems.

Acknowledgements

This work was supported by the Ministry of Health, Labor, and Welfare of Japan and by both the JST CREST program and Grant-in-Aid of the Ministry of Education, Culture, Sports, Science, and Technology of Japan. Y. Harada, T. Yamamoto, and M. Yokoyama acknowledge the support from the Program for Promoting the Establishment of Strategic Research Centers, Special Coordination Funds for Promoting Science and Technology, and the Ministry of Education, Culture, Sports, Science and Technology of Japan. We thank Asylum Technology Co., LTD., Tokyo, Japan for providing access to an Atomic Force Microscopy MFP-3D.

References

Aliabadi, H.M., Lavasanifar, A., 2006. Polymeric micelles for drug delivery. Expert Opin. Drug Deliv. 3, 139–162.

Bader, H., Ringsdorf, H., Schmidt, B., 1984. Watersoluble polymers in medicine. Angew. Chem. 123/124, 457–485.

Chansri, N., Kawakami, S., Yokoyama, M., Yamamoto, T., Charoensit, P., Hashida, M., 2008. Anti-tumor effect of all-*trans* retinoic acid loaded polymeric micelles in solid tumor bearing mice. Pharm. Res. 25, 428–434.

Forrest, M.L., Won, C.Y., Malick, A.W., Kwon, G.S., 2006a. In vitro release of the mTOR inhibitor rapamycin from poly(ethylene glycol)-*b*-poly(ε-caprolactone) micelles. J. Contr. Rel. 110, 370–377.

Forrest, M.L., Zhao, A., Won, C.Y., Malick, A.W., Kwon, G.S., 2006b. Lipophilic prodrugs of Hsp90 inhibitor geldanamycin for nanoencapsulation in poly(ethylene glycol)-*b*-poly(ε-caprolactone) micelles. J. Contr. Rel. 116, 139–149.

Hamaguchi, T., Matsumura, Y., Suzuki, M., Shimizu, K., Goda, R., Nakamura, I., Nakatomi, I., Yokoyama, M., Kataoka, K., Kakizoe, T., NK105, 2005. A paclitaxel-incorporating micellar nanoparticle formulation, can extend in vivo antitumour activity and reduce the neurotoxicity of paclitaxel. Br. J. Cancer 92, 1240–1246.

Hamaguchi, T., Kato, K., Yasui, H., Morizane, C., Ikeda, M., Ueno, H., Muro, K., Yamada, Y., Okusaka, T., Shirao, K., Shimada, Y., Nakahama, H., Matsumura, Y., 2007. A phase I and pharmacokinetic study of NK105, a paclitaxel-incorporating micellar nanoparticle formulation. Br. J. Cancer 97, 170–176.

Huynh, L., Grant, J., Leroux, J.-P., Delmas, P., Allen, C., 2008. Predicting the solubility of the anti-cancer agent docetaxel in small molecule excipients using computational methods. Pharm. Res. 25, 147–157.

Kawano, K., Watanabe, M., Yamamoto, T., Yokoyama, M., Opanasopit, P., Okano, T., Maitani, Y., 2006. Enhanced antitumor effect of camptothecin loaded in long-circulating polymeric micelles. J. Contr. Rel. 112, 329–332.

Hansen, C.M., 2007. Hansen Solubility Parameters; A User's Handbook, second ed. CRC Press, Boca Raton.

Koizumi, F., Kitagawa, M., Negishi, T., Onda, T., Matsumoto, S., Hamaguchi, T., Matsumura, Y., 2006. Novel SN-38-incorporating polymeric micelles, NK012, eradicate vascular endothelial growth factor-secreting bulky tumors. Cancer Res. 66, 10048–10056.

Kwon, G.S., Naito, M., Kataoka, K., Yokoyama, M., Sakurai, Y., Okano, T., 1994a. Block copolymer micelles as vehicles for hydrophobic drugs. Colloids Surf. B: Biointerf. 2, 429–434.

Kwon, G.S., Suwa, S., Yokoyama, M., Okano, T., Sakurai, Y., Kataoka, K., 1994b. Enhanced tumor accumulation and prolonged circulation times of micelle-forming poly(ethylene oxide–aspartate) block copolymer–adriamycin conjugates. J. Contr. Rel. 29, 17–23.

Maeda, H., Seymour, L.W., Miyamoto, Y., 1992. Conjugates of anticancer agents and polymers: Advantages of macromolecular therapeutics in vivo. Bioconjugate Chem. 3, 351–361.

Matsumura, Y., Maeda, H., 1986. A new concept for macromolecular therapeutics in cancer chemotherapy: Mechanism of tumoritropic accumulation of proteins and the antitumor agent smancs. Cancer Res. 46, 6387–6392.

Matsumura, Y., Hamaguchi, T., Ura, T., Muro, K., Yamada, Y., Shimada, Y., Shirao, K., Okusaka, T., Ueno, H., Ikeda, M., Watanabe, N., 2004. Phase I clinical trial and pharmacokinetic evaluation of NK911, a micelle-encapsulated doxorubicin. Br. J. Cancer 91, 1775–1781.

Molavi, O., Ma, Z., Mahmud, A., Alshamsan, A., Samuel, J., Lai, R., Kwon, G.S., Lavasanifar, A., 2008. Polymeric micelles for the solubilization and delivery of STAT3 inhibitor cucurbitacins in solid tumors. Int. J. Pharm. 347, 118–127.

Nakajima, T.E., Yanagihara, K., Takigahira, M., Yasunaga, M., Kato, K., Hamaguchi, T., Yamada, Y., Shimada, Y., Mihara, K., Ochiya, T., Matsumura, Y., 2008a. Antitumor effect of SN-38-releasing polymeric micelles, NK012, on spontaneous peritoneal metastases from orthotopic gastric cancer in mice compared with irinotecan. Cancer Res. 68, 9318–9322.

Nakajima, T.E., Yasunaga, M., Kano, Y., Koizumi, F., Kato, K., Hamaguchi, T., Yamada, Y., Shirao, K., Shimada, Y., Matsumura, Y., 2008b. Synergistic antitumor activity of the novel SN-38-incorporating polymeric micelles, NK012, combined with 5-fluorouracil in a mouse model of colorectal cancer, as compared with that of irinotecan plus 5-fluorouracil. Int. J. Cancer 122, 2148–2153.

Nishiyama, N., Okazaki, S., Cabral, H., Miyamoto, M., Kato, Y., Sugiyama, Y., Nishio, K., Matsumura, Y., Kataoka, K., 2003. Novel cisplatin-incorporated polymeric micelles can eradicate solid tumors in mice. Cancer Res. 63, 8977–8983.

Okuda, T., Kawakami, S., Yokoyama, M., Yamamoto, T., Yamashita, F., Hashida, M., 2008. Block copolymer design for stable encapsulation of N-(4-hydroxyphenyl)retinamide into polymeric micelles in mice. Int. J. Pharm. 357, 318–322.

Okuda, T., Kawakami, S., Higuchi, Y., Satoh, T., Oka, Y., Yokoyama, M., Yamashita, F., Hashida, M., 2009. Enhanced in vivo antitumor efficacy of fenretinide encapsulated in polymeric micelles. Int. J. Pharm. 373, 100–106.

Opanasopit, P., Yokoyama, M., Watanabe, M., Kawano, K., Maitani, Y., Okano, T., 2004. Block copolymer design for camptothecin incorporation into polymeric micelles for passive tumor targeting. Pharm. Res. 21, 2003–2010.

Shin, H.C., Alani, A.W., Rao, D.A., Rockich, N.C., Kwon, G.S., 2009. Multi-drug loaded polymeric micelles for simultaneous delivery of poorly soluble anticancer drugs. J. Contr. Rel. 140, 294–300.

Tuzar, Z., Kratochvil, P., 1976. Block and graft copolymer micelles in solution. Adv. Colloid Interf. Sci. 6, 201–232.

Yamamoto, Y., Yokoyama, M., Opanasopit, P., Hayama, A., Kawano, K., Maitani, Y., 2007. What are determining factors for stable drug incorporation into polymeric micelle carriers? Consideration on physical and chemical characters of the micelle inner core. J. Contr. Rel. 123, 11–18.

Yokoyama, M., Inoue, S., Kataoka, K., Yui, N., Okano, T., Sakurai, Y., 1989. Molecular design for missile drug: Synthesis of adriamycin conjugated with IgG using poly(ethylene glycol)-poly(aspartic acid) block copolymer as intermediate carrier. Die Makromolekulare Chemie 190, 2041–2054.

Yokoyama, M., Okano, T., Sakurai, Y., Ekimoto, H., Shibazaki, C., Kataoka, K., 1991. Toxicity and antitumor activity against solid tumors of micelle-forming polymeric anticancer drug and its extremely long circulation in blood. Cancer Res. 51, 3229–3236.

Yokoyama, M., Okano, T., Sakurai, Y., Kataoka, K., 1994. Improved synthesis of adriamycin-conjugated poly(ethylene oxide)-poly(aspartic acid) block copolymer and formation of unimodal micellar structure with controlled amount of physically entrapped adriamycin. J. Contr. Rel. 32, 269–277.

Yokoyama, M., Okano, T., Sakurai, Y., Fukushima, S., Okamoto, K., Kataoka, K., 1999. Selective delivery of adriamycin to a solid tumor using a polymeric micelle carrier system. J. Drug Targeting 7, 171–186.

Yokoyama, M., Opanasopit, P., Maitani, Y., Kawano, K., Okano, T., 2004. Polymer design and incorporation method for polymeric micelle carrier system containing water-insoluble anti-cancer agent camptothecin. J. Drug Targeting 12, 373–384.

Yokoyama, M., 2005. Polymeric Micelles for the Targeting of Hydrophobic Drugs. In: Kwon, G.S. (Ed.), Drug and Pharmaceutical Sciences, Vol. 148, Polymeric Drug Delivery Systems. Taylor & Francis, Boca Raton, pp. 533–575.

Yokoyama, M., 2007. Polymeric micelles as nano-sized drug carrier systems. In: Domb, A.J., Tabata, Y., Kumar, M.N.V.R., Farber, S. (Eds.), Nanoparticles for Pharmaceutical Applications. American Scientific Publishers, Stevenson Ranch, pp. 63–72.

Watanabe, M., Kawano, K., Yokoyama, M., Opanasopit, P., Okano, T., Maitani, Y., 2006. Preparation of camptothecin-loaded polymeric micelles and evaluation of their incorporation and circulation stability. Int. J. Pharm. 308, 183–189.

Journal of Nuclear Medicine, published on April 15, 2011 as doi:10.2967/jnumed.110.084848

Experimental Pig Model of Old Myocardial Infarction with Long Survival Leading to Chronic Left Ventricular Dysfunction and Remodeling as Evaluated by PET

Noboru Teramoto[1], Kazuhiro Koshino[1], Ikuo Yokoyama[2,3], Shigeru Miyagawa[4], Tsutomu Zeniya[1], Yoshiyuki Hirano[1], Hajime Fukuda[1], Junichiro Enmi[1], Yoshiki Sawa[4], Juhani Knuuti[5], and Hidehiro Iida[1]

[1]Department of Investigative Radiology, National Cerebral and Cardiovascular Center Research Institute, Osaka, Japan; [2]School of Medicine and Faculty of Medicine, The University of Tokyo, Tokyo, Japan; [3]Department of Cardiovascular Medicine, Sanno Hospital, International University of Health and Welfare, Tokyo, Japan; [4]Department of Cardiac Surgery, Osaka University, School of Medicine, Osaka, Japan; and [5]Turku PET Centre, University of Turku, Turku, Finland

A pig model of reduced left ventricular (LV) function and remodeling or chronic heart failure with long survival after myocardial infarction (MI) has not been established. The aim of this study was to evaluate the pathophysiologic status of a pig model of old MI using a series of PET studies. **Methods:** Twenty-seven male farm pigs were divided into 2 groups: 7 animals in the control group and 20 animals that underwent a proximal coronary artery (CA) occlusion using an ameroid constrictor after distal CA ligation. A series of PET examinations was performed to assess LV volumes, LV functions, myocardial perfusion response to adenosine, and viability as water-perfusable tissue index. **Results:** The distal CA ligation inhibited arrhythmia during and after the operation, and a transmural anteroseptal MI, with an infarction area of 27% ± 5% of the whole left ventricle, was generated with a survival rate of 75% at 4 mo. Wall motion evaluated by ^{18}F-FDG PET was diffusely reduced, including the noninfarcted wall. Global LV ejection fraction as assessed by gated C^{15}O PET was reduced (39% ± 16%) in the group undergoing occlusion, compared with the control group (66% ± 16%, $P < 0.05$). LV end-systolic (31.4 ± 9.2 cm^3) and end-diastolic (52.7 ± 10.2 cm^3) volumes were increased, compared with controls (15.2 ± 9.4 cm^3, $P < 0.01$, and 41.7 ± 11.5 cm^3, $P < 0.05$, respectively). Histology showed hypertrophy and development of microscopic fibrosis in noninfarcted myocardium. PET demonstrated the reduced myocardial perfusion response to adenosine and also reduced water-perfusable tissue index in remote segments. **Conclusion:** The pig model of old MI generated by the chronic proximal CA obstruction after distal ligation was characterized by LV dysfunction and remodeling, with a high survival rate.

Key Words: experimental model; PET; myocardial flow reserve; remodeling; regeneration therapy

J Nucl Med 2011; 52:761–768
DOI: 10.2967/jnumed.110.084848

Chronic heart failure (CHF) is an increasing health concern (*1*). Myocardial infarction (MI) is the cause of CHF in two thirds of the patients, and the morbidity and mortality remain high (*2,3*). The potential therapies, such as new class of pharmacologic agents and cell therapy (*4*), need to be tested in proper animal models to demonstrate the effects and outcome before initiating clinical trials. Dogs have been extensively used in heart research. Because the coronary arterial systems in dogs can develop collaterals quickly when myocardial ischemia occurs, it has been difficult to produce a large MI that typically introduces CHF with general characteristics of left ventricular (LV) remodeling (*5*).

Pigs have been considered better suited than dogs for pathophysiologic research of ischemic heart diseases, because the coronary system of pigs is more similar to that of humans (*6*). Tolerance of ischemia and denervation after ischemia in pigs is also similar to that in humans (*6*). Because of the delayed development of collaterals after occlusion, ligation of a peripheral part of the coronary arterial system generates a small MI (*7*). However, an experimental model of large MI introducing global LV dysfunction is difficult to develop, because sudden cardiac death (SCD) due to fatal arrhythmias and an intolerance of ischemia frequently occurs in pigs (*8*). The models of small MI made by the ligation of a peripheral part of the coronary arterial system demonstrate reasonably good survival rates but only for a small infarction. The model of small MI using a coronary ameroid constrictor (model MRI-2.50-TI; Research Instruments SW) has also demonstrated moderate SCD rates (*6,8–13–15*), but the animals develop primarily chronic ischemia or hibernating myocardium, without a significant amount of scar tissue. Thus, the limitations of current models are that the infarcted region is small and that the hearts are not developing a clinical picture of CHF with global LV dysfunction, LV dilatation, and remodeling.

On the other hand, Shen et al. (*16*) developed an experimental pig model of MI and heart failure. Sequential

Received Oct. 30, 2010; revision accepted Dec. 9, 2010.
For correspondence or reprints contact: Hidehiro Iida, Department of Investigative Radiology, National Cardiovascular Center Research Institute, 5-7-1 Fujishiro-dai, Suita City, Osaka, Japan 565-8565.
E-mail: iida@ri.ncvc.go.jp

ligation of distal and proximal coronary arteries was used to establish MI with a reasonable survival rate, and pacing tachycardia was used to achieve heart failure. However, this pig model was studied over only a short term (21 d) and required pacing tachycardia to cause CHF. There has been little evaluation of pathophysiology and no evidence of the presence of cardiac remodeling.

This aim of this study was to characterize the pig model of old MI. We first reinvestigated the technique of generating a pig model of relatively large MI causing global LV dysfunction and LV remodeling in segments remote from the infarcted region, by means of the sequential ligation of distal and proximal coronary arteries without the pacing procedures. We then evaluated the pathophysiologic characteristics of this animal model by comprehensively analyzing histology, LV volumes and LV function, myocardial perfusion response to adenosine, and perfusable tissue fractions (PTF) in the remote segment, using an advanced PET technique.

MATERIALS AND METHODS

Subjects

Male farm pigs, 3 mo old at the start of the study (weight range, 18–23 kg; mean weight ± SD, 20 ± 1.2 kg), were used. The animals were divided into 2 groups. Group A consisted of 7 pigs without any operation and was designated as the control group (average body weight, 26 ± 2.4 kg). Group B consisted of 20 pigs that underwent occlusion using an ameroid constrictor (*7*); ligation of the distal left anterior descending coronary artery (LAD) was performed before the ameroid constrictor was used. Of the 16 pigs that survived for 4 mo after the operation, 7 underwent PET studies. The other 9 were assigned to tissue-regenerative projects. The average body weight of this group of 7 pigs was 42 ± 8.2 kg at the time of the PET scan.

Animals were maintained and handled in accordance with guidelines for animal research (*17*). The study protocol was approved by the local Committee for Laboratory Animal Welfare, National Cardiovascular Center, Osaka, Japan.

Permanent Occlusion Procedures

In group B, permanent occlusion was made at the proximal LAD using an ameroid constrictor (*18*) (Fig. 1) as follows. Pigs were preanesthetized by an intramuscular injection of ketamine hydrochloride (20 mg/kg; Ketaral [Diichi-Sankyo]) and xylazine hydrochloride (2 mg/kg; Celactal [Bayer HealthCare]). The animals were positioned supine, and a 22-gauge indwelling needle (Surflo F&F; Terumo) was inserted in the central vein of the auricle. A 3-way cock (Terufusion TS-TR2K; Terumo) was attached to the external cylinder of the indwelling needle and connected for continuous anesthetic injection. The animals were intubated with an endotracheal cannula (6 French; Sheridan) and then connected to an artificial respirator (Single Animal Volume Controlled Ventilators model 613 [Harvard Apparatus]) with a stroke volume of 200–300 cm^3/stroke and frequency of 20/min. Propofol (6 mg/kg/h; Diprivan [Astra-Zeneca]) and vecuronium bromide (0.05 mg/kg/h; Musculux [Sankyo Yell Yakuhin Co., Ltd.]) were continuously infused using a syringe pump (Terufusion TE-3310N; Terumo). Then, the animals were fixed in a recumbent position so that the left thorax was exposed, and the outer layer of skin and muscles between the third and fourth ribs was dissected. The distance between the third and fourth ribs was widened with a rib spreader to allow a direct view of the left auricle and LAD. The pericardium was dissected along the LAD, from the upper part of the left auricle (~6 cm), to expose the myocardium around the LAD. The LAD on the proximal side, below the left auricle from the myocardium, was exfoliated for approximately 1 cm. A lidocaine hydrochloride jelly (Xylocaine jelly; Astra-Zeneca) was applied to anesthetize the area.

A complete ligation was first made on the distal LAD (no. 9), immediately after the second diagonal branch, using a suture (2-0; Nescosuture) approximately 20 min before the ameroid constrictor was fastened. An ameroid constrictor (COR-2.50-SS; Research Instruments) was then fastened using sutures as displayed in Figure 1. To enhance the effect of the ameroid constrictor, 2 additional suture strings were loosely rounded at the site of the ameroid so that these strings were located between (below) the ameroid constrictor and arterial wall.

PET Procedures

After fasting overnight, the pigs were sedated with ketamine hydrochloride (20 mg/kg) and xylazine hydrochloride (2 mg/kg) by intramuscular injection. Anesthesia was induced and maintained with intravenous propofol (6 mg/kg/h) and vecuronium bromide (0.05 mg/kg/h). The animals were intubated and mechanically ventilated with a mixture of 25% oxygen and 75% nitrogen at 10 mL/kg plus 50 mL/stroke at 20 strokes/min. Catheters were placed in the femoral artery to monitor the arterial blood pressure and in the femoral vein to infuse $H_2{}^{15}O$ or ^{18}F-labeled FDG. Systolic and diastolic blood pressure, heart rate, and arterial blood gases were monitored.

A series of PET scans was obtained using an ECAT-HR tomograph (CTI Inc.). The blood-pool images were obtained after the animals inhaled 2.7 GBq of $C^{15}O$ gas (*19*). Arterial blood samples were taken every minute during the $C^{15}O$ scan, and their radioactivity concentration in the whole blood was measured. Additional electrocardiogram-gated $C^{15}O$ images were obtained (16 gates). After 12–15 min of ^{15}O radioactivity decay, 7 dynamic $H_2{}^{15}O$ PET scans were acquired at intervals of 12–15 min. The first and the last scans were obtained without pharmacologic stress, and the second through sixth scans were obtained during intravenous infusion of adenosine (100, 200, 400, 600, and 800

[Fig. 1]

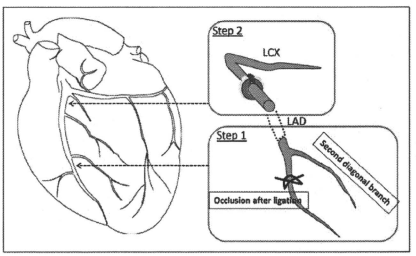

RGB

FIGURE 1. Ligation of LV LAD. Distal LAD after second diagonal branch was ligated, and 30 min later ameroid constrictor was placed at proximal LAD. Two suture strings were inserted between ameroid constrictor and arterial wall to make occlusion complete. LCX = left circumflex artery.

jnm084848-pm 32 ■ 4/15/11

[only for group A] μg/kg/min). The 6-min dynamic scan of 26 frames (12 × 5, 8 × 15, and 6 × 30 s) was started when radioactivity appeared in the right ventricle. Furthermore, another PET scan using ^{18}F-FDG was acquired using a euglycemic hyperinsulinemic clamp (*20,21*). For this study, insulin (4 mIU/kg/h) and glucose (5–8 mg/kg/min) were continuously infused over 2 h, and then approximately 111 MBq of ^{18}F-FDG was intravenously injected. The blood glucose was 109 ± 10.6, 105 ± 3.8, and 107 ± 10.0 mg/dL at the time of ^{18}F-FDG injection. PET images were acquired dynamically for 60 min, and the images acquired during the last 30 min were used for further analysis. An additional electrocardiogram-gated scan was obtained for 30 min to estimate myocardial wall motion and wall thickening.

After the PET scans, coronary angiography was undertaken to confirm the occlusion of LAD. A portable angiographic camera (Digital Mobile Imaging System OEC Series 9800; GE Healthcare U.K. Ltd.) was used with the contrast medium (Omnipaque 300; Daiichi-Sankyo).

Histologic Analysis

At the end of the study, pentobarbital sodium was administered, and animals were euthanized. The animals' hearts were then excised and sliced at a thickness of 10 mm to correspond to PET images (*22*). The slices were stained with Masson trichrome and hematoxylin and eosin. The surface area of the infarcted LV wall on the stained slices was calculated according to a previously describe procedure (*22*). The length of the infarcted zone, including both transmural and nontransmural infarction, was measured on each of the stained slices along the LV wall. The defect surface area was then calculated as a summation of the defect length multiplied by the slice interval. The cell and microvascular structures were also analyzed. In particular, development of fibrosis, cell enlargement, and degeneration of the vascular network were visually estimated. The analysis was masked from the other analyses.

Data Analysis

The extravascular tissue density images (g/mL) were calculated by subtracting the $C^{15}O$ blood volume from the transmission images (*23*). The relative images of myocardial blood flow (MBF) and water-PTF (g/mL) were also generated from the dynamic $H_2{}^{15}O$ images (*22,23*). The relative accumulation of ^{18}F-FDG was calculated using validated techniques (*24*). The regions of interest were placed in the anterior wall and lateral–anterior wall, which corresponded to the MI and normal-tissue regions, respectively. The regions of interest were then copied to other images, and the quantitative parameters of regional MBF (mL/min/g), PTF (g/mL), and arterial blood volume V_a (mL/mL) were calculated using nonlinear least-squares fitting as described previously (*22,23*). These calculations were done for all $H_2{}^{15}O$ PET studies to estimate baseline MBF and the adenosine-based responses both in MI and in non-MI regions.

The water-perfusable tissue index (PTI) (*23,25,26*), which was defined as the fraction of water-perfusable tissue over total tissue, was calculated by dividing PTF by the extravascular tissue density images. This calculation was done for each myocardial region and compared between the infarcted anterior wall and normal posterior–lateral wall regions. The obtained values were also compared with control subjects.

The LV ejection fraction and cardiac output were evaluated by counting the total counts within the LV area from the typical electrocardiogram-gated $C^{15}O$ images shown in Figure 2. The wall motion was analyzed using electrocardiogram-gated ^{18}F-FDG images. The wall motion score was divided into 4 levels (normal, 0; hypokinetic, 1; akinetic, 2; and dyskinetic, 3) and defined for the anterior wall and contralateral (lateral–posterior) wall regions. [Fig. 2]

The surface area of the infarcted LV wall on the ^{18}F-FDG and PTF images was calculated as described previously (*22*). A significant defect was defined as a value less than 50% of that in the control region, which was defined in the contralateral region, indicating preserved ^{18}F-FDG, preserved PTF, and elevated MBF during adenosine. The myocardial midlines were then traced along the 50% of peak count boundary of the $C^{15}O$ blood volume images at each slice (*22*). The surface area of the defect was calculated as a summation of the defect length multiplied by the slice interval. These defect surface areas were compared with those obtained from the stained slices.

All data were presented as mean ± SD. Pearson correlation and linear regression analyses were used to evaluate relationships between the 2 values. A P value of less than 0.05 was considered statistically significant.

RESULTS

Survival Rates of Animal Groups

No adverse events were detected in group A; in group B, 4 pigs (20%) died within a month and an additional pig 1 mo after that. Thus, the total survival rate at 4 mo was 75% in group B. Severe arrhythmia occurred in all animals in group B during the operation. The arrhythmia and fibrillation, introducing the sudden cardiac death, were significantly suppressed at approximately 20 min after ligation of the distal LAD. Figure 3 displays the survival rates of the pigs that underwent the operation. [Fig. 3]

Of the pigs in group B that survived for 4 mo, 7 were selected for further characterization and imaging studies. These 7 animals were compared against the animals in group A, on which no operation was performed. The characteristics of the 2 groups at the time of the imaging

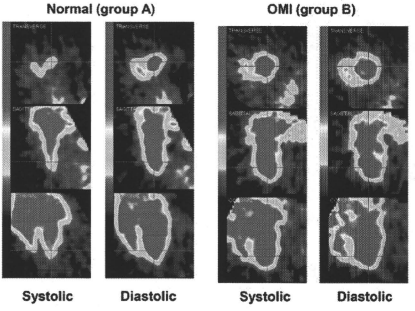

RGB

FIGURE 2. Typical images obtained from electrocardiogram-gated PET scans with $C^{15}O$ inhalation at end-systolic and end-diastolic phases. OMI = old MI.

33
jnm084848-pm ■ 4/15/11

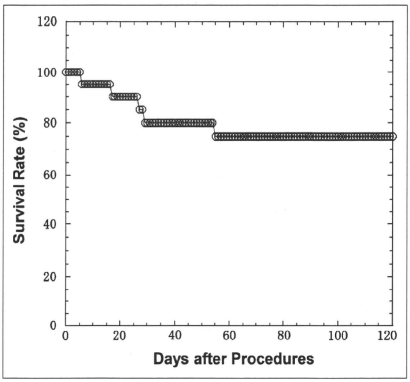

FIGURE 3. Survival rates for group B after ameroid constrictor was placed.

[**Table 1**] studies are displayed in Table 1. Because the animals in group B were allowed to grow after operation, they were larger at the time of the imaging studies.

Characteristics of Groups

Table 1 shows the hemodynamic data for the animals in groups A and B. Compared with group A, group B showed a significantly reduced heart rate and diastolic blood pressure and, thus, rate–pressure product. In addition, the global LV ejection fraction measured with gated $C^{15}O$ PET in group B was significantly reduced (39% ± 16% [24%–59%] in group B vs. 66% ± 16% [46%–91%] in group A, $P < 0.01$). LV end-systolic volume in group B was significantly increased (31.4 ± 9.2 cm^3 in group B vs. 15.2 ± 9.4 cm^3 in group A, $P < 0.01$), and LV end-diastolic volume was also significantly increased (52.7 ± 10.2 cm^3 in group B vs. 41.7 ± 11.5 cm^3 in group A, $P < 0.05$). Increased end-systolic and end-diastolic volumes are also clearly visible in Figure 2. Systolic blood pressure and diastolic blood pressure, as well as rate–pressure product, were reduced during adenosine study in both groups. Heart rate was increased in group A but not in group B. Other parameters such as hemoglobin concentration (g/dL), percentage saturation of arterial O_2, $PaCO_2$ (mm Hg), and PO_2 (mm Hg) were not significantly different between the 2 groups. Table 2 shows detailed hemodynamic parameters [**Table 2**] and the results from the histologic analysis for each individual animal in group B. Wall motion score was reduced (akinesis–dyskinesis or 2–3) in the anterior wall, which includes the area of MI. The wall motion score was also reduced diffusely in all animals and indicated hypokinesis (grade 1) in the infarct-remote posterolateral wall. The coronary angiography demonstrated complete occlusion of the LAD in all animals in group B. As shown in Figure 4, no [**Fig. 4**] clear collateral circulation existed.

Imaging Results

The myocardial perfusion ($H_2{}^{15}O$) and metabolism (^{18}F-FDG) images at the mid ventricular plane and their corresponding slices after histochemical staining for the animals in group B are displayed in Figure 5. In all animals, clear [**Fig. 5**] signs of MI were detected in the anterior wall. The surface area of the MI was 13.7 ± 4.3 cm^2, which corresponded to 27% ± 9% of the whole left ventricle. Both PTF and ^{18}F-FDG images visually agreed well with the stained slices. Moreover, the ^{18}F-FDG images agreed well with the qualitative PTF images in all animals. The spatial distribution and size of the developed MI are visually reproducible

TABLE 1
Physiologic Parameters of Pigs at Time of PET

Parameter	Group A (control, n = 7)	Group B (old MI, n = 7)
Body weight (kg)	26 ± 2.4	41 ± 8.2
Heart rate (beats·min^{-1})	72 ± 22.4 (82 ± 21.4*)	52 ± 6.3† (53 ± 9.2)
Systolic blood pressure (mm Hg)	131 ± 22.1 (95 ± 22.4‡)	111 ± 18.3† (97 ± 15.0*)
Diastolic blood pressure (mm Hg)	92 ± 19.3 (49 ± 16.7‡)	74 ± 13.6† (57 ± 11.9‡)
Rate pressure product (mm Hg·min^{-1})	9,567 ± 3,616 (5,657 ± 3201‡)	5,732 ± 1,151† (4,445 ± 948*)
Wall thickness (posterior–lateral wall) (cm)	1.2 ± 0.1	1.6 ± 0.1‡
End-diastolic LV volume (mL)	41.7 ± 11.5	52.73 ± 10.2†
End-systolic LV volume (mL)	15.2 ± 9.4	31.4 ± 9.2*
LV ejection fraction (%)	66.0 ± 16.2	39.7 ± 16.9*
Hemoglobin concentration (g/dL)	13 ± 1.5	12 ± 0.9
Saturation of arterial O_2 (%)	99 ± 1.0	99 ± 0.6
pCO_2 (mm Hg)	39 ± 2.7	41 ± 2.8
pO_2 (mm Hg)	125 ± 20.1	141 ± 11.4

*$P < 0.01$.
†$P < 0.05$.
‡$P < 0.001$.
Data are mean ± SD. Values in parentheses are from administration of maximum dose of adenosine.

jnm084848-pm 34 ■ 4/15/11

TABLE 2
Hemodynamic Parameters of Pigs with Old MI (Group B)

Subject no.	BW (kg)	HR (beats·min^{-1})	SBP (mm Hg)	DBP (mm Hg)	RPP (mm Hg·min^{-1})	tHb (g/dL)	SAT (%)	pCO_2 (mm Hg)	pO_2 (mm Hg)	WM			EDV (mL)	ESV (mL)	EF (%)	LV surface area (cm^2)	MI surface area (cm^2)	DAF (%)
										Anterior wall	Posterior–lateral wall	WT (posterior–lateral wall)						
1	37	53	117	72	6,201	10.8	98.7	37.8	132	3	1	1.6	39.5	29.9	24.3	53.7	10.9	20.3
2	39	38	110	70	4,180	11.5	98.9	37	154.5	2	1	1.6	58.2	42.4	27.1	57	16.2	28.4
3	33	53	85	60	4,505	11.5	99.3	39.3	137.7	3	1	1.6	55.4	42.3	23.6	50	16	31.9
4	32	55	91	58	5,005	11.3	99.6	40.7	135.5	–	–	1.8	0	0	0	53.9	9.2	17.1
5	45	52	137	93	7,124	10.3	98.1	43.6	124.1	3	1	1.8	68.4	27.6	59.7	50	19.9	39.7
6	50	52	126	90	6,552	11.8	99.7	42.8	148.4	3	1	1.5	49.3	27.1	45	48.6	15.5	31.8
7	53	58	113	78	6,554	13.3	99	43.7	152.8	2	1	1.5	45.7	19.1	58.2	49.8	8.4	16.9
Mean	41	52	111	74	5,732	12	99	41	141	2.7	1	1.6	52.7	31.4	39.7	51.9	13.7	26.6
SD	8.2	6.3	18.3	13.6	1,151	0.9	0.6	2.8	11.4	0.5	0	0.1	10.2	9.2	16.9	3.05	4.3	8.7

BW = body weight; HR = heart rate; SBP = systolic blood pressure; DBP = diastolic blood pressure; RPP = rate–pressure product; tHB = hemoglobin concentration; SAT = saturation of arterial O_2; WM = wall motion; WT = wall thickness; EDV = end-diastolic LV volume; ESV = end-systolic LV volume; EF = ejection fraction; DAF = defect area fraction.

RGB

FIGURE 4. Example of coronary angiogram in animal with ameroid constrictor (arrow) (group B).

among the animals. Myocardial hypertrophy was visible in the wall regions remote from the infarcted area. In group B, the posterior–lateral wall thickness estimated from histochemical staining was 16 ± 1 mm (Table 2), which was significantly greater than that of group A (12 ± 1 mm; Table 1) ($P < 0.001$).

Further analysis of the size of the infarcted region is displayed in Figure 5B. We excluded 1 animal whose ^{18}F-FDG PET images demonstrated high accumulation at the anterior LV area (and therefore a smaller value in the defect surface area), which was attributed to the adhesion or inflammation between the myocardial and chest walls. Thus, the defect area on histology showed intersubject variation of approximately 20%. The results of both ^{18}F-FDG and PTF image analysis and histochemical analysis agreed well (Fig. 5B). Baseline and adenosine-stimulated MBF were also clearly blunted in the anterior wall in the animals in group B (Fig. 6A). Interestingly, abnormally reduced adenosine flow response also was detected in the myocardial regions remote from the MI in group B, whereas the baseline flow values were normal. [Fig. 6]

Further analysis of myocardial PTF and PTI values—indices of PTF—revealed that these values were significantly reduced in the infarcted anterior wall in group B (Fig. 6B). PTI was also moderately but significantly (~10%) reduced in the remote myocardial wall in group B.

Histologic Analysis

Histologic analysis did not show any signs of MI in group A, but transmural anterior wall MI was apparent in all animals in group B. Hypertrophy was detected in the posterior wall of group B in all animals. Multinuclear muscle cell breeding (Fig. 7A) and hyperplasia of blood vessels (Fig. 7B) were also visible in all animals in group B, mostly in the subendocardial regions. Denaturation necrosis with epicardial fibrous change and hypertrophy has also been seen in the lateral–posterior wall regions of group B (Fig. 7C). [Fig. 7]

DISCUSSION

This study demonstrated that 75% of pigs with old MI generated by the 2 steps of LAD ligation survived more than 4 mo. Such a long survival has never, to our

jnm084848-pm 35 ■ 4/15/11